Journal of Atmospheric and Solar-Terrestrial Physics ▮ (▮▮▮▮) ▮▮▮–▮▮▮

Contents lists available at ScienceDirect

Journal of Atmospheric and Solar-Terrestrial Physics

journal homepage: www.elsevier.com/locate/jastp

Three-dimensional reconstruction of coronal mass ejections using heliospheric imager data

Timothy A. Howard *

Department of Space Studies, Southwest Research Institute, 1050 Walnut St, Boulder, CO 80302, USA

ARTICLE INFO

Article history:
Received 29 January 2010
Received in revised form
13 July 2010
Accepted 6 August 2010

Keywords:
Sun
Coronal mass ejections
Heliospheric imaging
Space weather

ABSTRACT

Innovative techniques have been developed to extract three-dimensional (3-D) information on coronal mass ejections. Some techniques have only been available since the launch of the STEREO spacecraft, where geometry can be applied to white light observations from three different viewpoints. Another technique not necessarily requiring the multiple-viewpoint capabilities of STEREO involves heliospheric imaging. With heliospheric imagers, we may take advantage of the breakdown in geometrical and Thomson scattering linearity and, with careful analysis of the data, extract 3-D parameters from CME images. In this review we discuss the various techniques that are being developed and used to reconstruct the 3-D structure and kinematic evolution of CMEs, with a particular emphasis on the work of the author and colleagues. Following a brief review of multiple-viewpoint coronagraph analysis, we focus on techniques involving heliospheric images, which can be used to achieve the reconstruction with a good degree of accuracy without the need for auxiliary data.

1. Introduction

Coronal mass ejections (CMEs) are large eruptions of plasma and magnetic field from the Sun. They may contain masses in excess of 10^{13} kg and early in their evolution they can achieve speeds in excess of 3000 km/s. CMEs are believed to be responsible for the removal of large quantities of magnetic energy and plasma from the solar atmosphere (Low, 1996), and a single CME contains more energy than all of the other solar eruptive phenomena (e.g. flares, solar energetic particles) combined (Emslie et al., 2004). They are hence an important mechanism in solar cycle evolution. Upon their occasional impact with the Earth they compress the magnetosphere and may inject large quantities of energetic particles resulting in large disturbances known as (geo)magnetic storms (e.g. Dungey, 1961, 1963). Magnetic storms are responsible for a variety of damage to technological infrastructure on and near the Earth, including power station damage, communications disruption, spacecraft damage and destruction and increased radiation dosage to aircraft passengers and astronauts. The NRC report by Baker et al. (2009) provides a review of the status quo regarding space weather. Improving our understanding of CMEs is hence of great significance to both scientific and technological objectives.

CMEs are very faint relative to the brightness of the Sun, and so they have traditionally been observed using white light coronagraphs that block out the photospheric light using an occulting disk, revealing the faint surrounding corona. These coronagraphs detect the Thomson scattered light off free electrons in the CME, and the most successful coronagraphs for CME detection have all been on spacecraft. This includes those on board OSO-7 (Tousey, 1973) and Skylab (Gosling et al., 1974), the later Solwind (Michels et al., 1980) and C/P on board SMM (MacQueen et al., 1980), and the more recent LASCO on SOHO (Brueckner et al., 1995) and the CORs on STEREO (Howard et al., 2008). Statistical studies on CMEs have been reported by many workers, including Hundhausen et al. (1994), St. Cyr et al. (2000), and Yashiro et al. (2004).

1.1. Kinematic measurements of CMEs

From the early days of CME observations, measurements of height, speed and acceleration were obtained by measuring the location of the leading edge of the structure in the coronagraph relative to the center of the Sun. They provide a reasonable approximation of the location of the CME as it moves through the field of view of the coronagraph but are limited due to the physics by which the CME is observed in white light. Firstly the images are sky plane projections, and so measurements of distance do not represent the actual three-dimensional (3-D) distance of the structure, but rather this distance projected into the sky plane. That is,

$$d_{\text{measured}} = d_{\text{actual}} \cos\Theta, \tag{1}$$

* Tel.: +1 720 240 0140; fax: +1 303 546 9687.
E-mail address: howard@boulder.swri.edu
URL: http://www.boulder.swri.edu/~howard/

1364-6826/$ - see front matter © 2010 Elsevier Ltd. All rights reserved.
doi:10.1016/j.jastp.2010.08.009

where Θ is the angle the central axis of the CME makes with the sky plane.

The other limitation of white light images is due to the Thomson scattering physics that enable us to detect them. These bias CME intensities to near the plane of the sky because at small angles from the Sun the scattered light is maximized (e.g. Andrews et al., 1998). Combining geometry and the scattering physics we may convert the angular separation into a physical distance by applying some simple, yet unavoidable approximations. These allow a simplified conversion to distance units but at the cost of removing 3-D information about the CME from the coronagraph images. Further from the Sun this linearity breaks down which increases the complexity of the required analysis, but enables the extraction of 3-D information.

This review discusses recent developments in the extraction of 3-D information on CMEs using coronagraph and heliospheric imager data alone. Such developments represent a great advance in the study of CMEs as the reliance on auxiliary data to identify 3-D information has led to misunderstanding and misinterpretation of CME data. We discuss the various techniques that are being developed and used to reconstruct the 3-D structure and kinematic evolution of CMEs, with a particular emphasis on the work of the author and colleagues. We begin with a brief review of techniques used to identify 3-D information about CMEs followed by a discussion of the utility of the stereoscopic capabilities of the STEREO coronagraphs to attempt 3-D reconstruction. We then move on to a discussion of heliospheric imagers and how they may be used to identify 3-D CME parameters by taking advantage of the breakdown of the linearity that occurs when CMEs are far from the Sun. We demonstrate that heliospheric image data alone may be utilized for fast, reliable and potentially accurate 3-D CME reconstruction without the need for auxiliary data or a stereoscopic viewpoint, and conclude that a replacement next generation heliospheric imager is urgently needed before the current imagers lose their capability for space weather forecasting.

2. Extracting three-dimensional information from coronagraphs

Workers in the past have attempted to identify 3-D properties of coronagraph CMEs using auxiliary data (i.e. solar "surface" features) as indicators. Such indicators take many forms, including active regions (e.g. Falconer et al., 2002), X-ray and Hα flares (e.g. Howard et al., 2008), disappearing filaments (erupting prominences) (e.g. Li and Luhmann, 2006) and post-eruptive arcades (Tripathi et al., 2004). These indicators are often labeled as the source or origin of the CME (e.g. Owens and Cargill, 2004; Gopalswamy, 2004, 2009; Wang et al., 2006; Gopalswamy et al., 2007), although this is incorrect. Solar flares, for example, have long been known to be associated with CMEs at only the secondary or tertiary level (Kahler, 1992; Gosling, 1993), with the timing of the flare not coincident with the onset of the CME (Harrison et al., 1985) and the location of the flare associated with just a single footpoint of the CME (Simnett and Harrison, 1984). Solar surface indicators are also limited because they do not provide information on changes to the CME during its evolution through the heliosphere (e.g. change of direction). Hence, the extraction of 3-D CME information using solar surface indicators have been met with limited success.

STEREO coronagraph data have for the first time provided a means to identify 3-D information from coronagraph data alone. This is because of the angular separation between both STEREO spacecraft and the Sun–Earth line, enabling the geometrical perspective to be recognized. When observed with coronagraphs, the CME is close enough to the Sun to enable the safe assumption that geometrical features commonly observed from different viewpoints are at the same location in 3-D space. Relative differences in the apparent structure of the CME can then be assumed to be entirely due to projection effects. Hence, by measuring the relative location of a number of common features observed on the CME from the CORs and LASCO we may apply simple geometrical triangulation to identify the 3-D location of each feature. Such a technique was performed by Howard and Tappin (2008) who identified the 3-D location of two CMEs observed by LASCO and the CORs in November 2007. Fig. 1 shows their Fig. 2c, showing the effects of projection on the same CME observed from two viewpoints. The CME in the COR2-A image on the left is narrower and further from the Sun than the CME in the COR2-B image on the right even though both images were obtained at the same time. This is because the location of this CME is closer to the plane of the sky of STEREO-A than STEREO-B.

Fig. 2 shows the location of both CMEs on the solar surface and in the ecliptic plane as determined by Howard and Tappin (2008) (their Fig. 5). The three traces on each solar image indicate the locations relative to LASCO (L) and COR2-A and B (A and B) at three locations, the northern and southern flanks, and the central point. The largest deviation between the three instruments was at the northern flank because there is a greater relative uncertainty when the measured point is closest to the same plane as the observers. The difference in longitude of the two events between

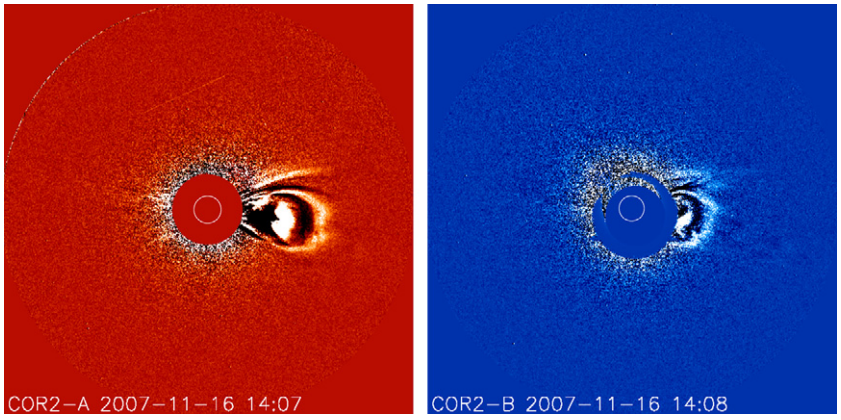

Fig. 1. Two STEREO/COR2 coronagraph images of a single CME obtained from two different viewpoints. Both images were taken on November 16, 2007 at 14:07 UT. At the time of these images, both STEREO were approximately 20° from the Sun–Earth line (and therefore 40° from each other), with STEREO-A (COR2-A, left) ahead and STEREO-B (COR2-B, right) behind. The solid disk in the center is the occulting disk and the white circle in both images represents the solar disk (Howard and Tappin, 2008).

Please cite this article as: Howard, T.A., Three-dimensional reconstruction of coronal mass ejections using heliospheric imager.... Journal of Atmospheric and Solar-Terrestrial Physics (2010), doi:10.1016/j.jastp.2010.08.009

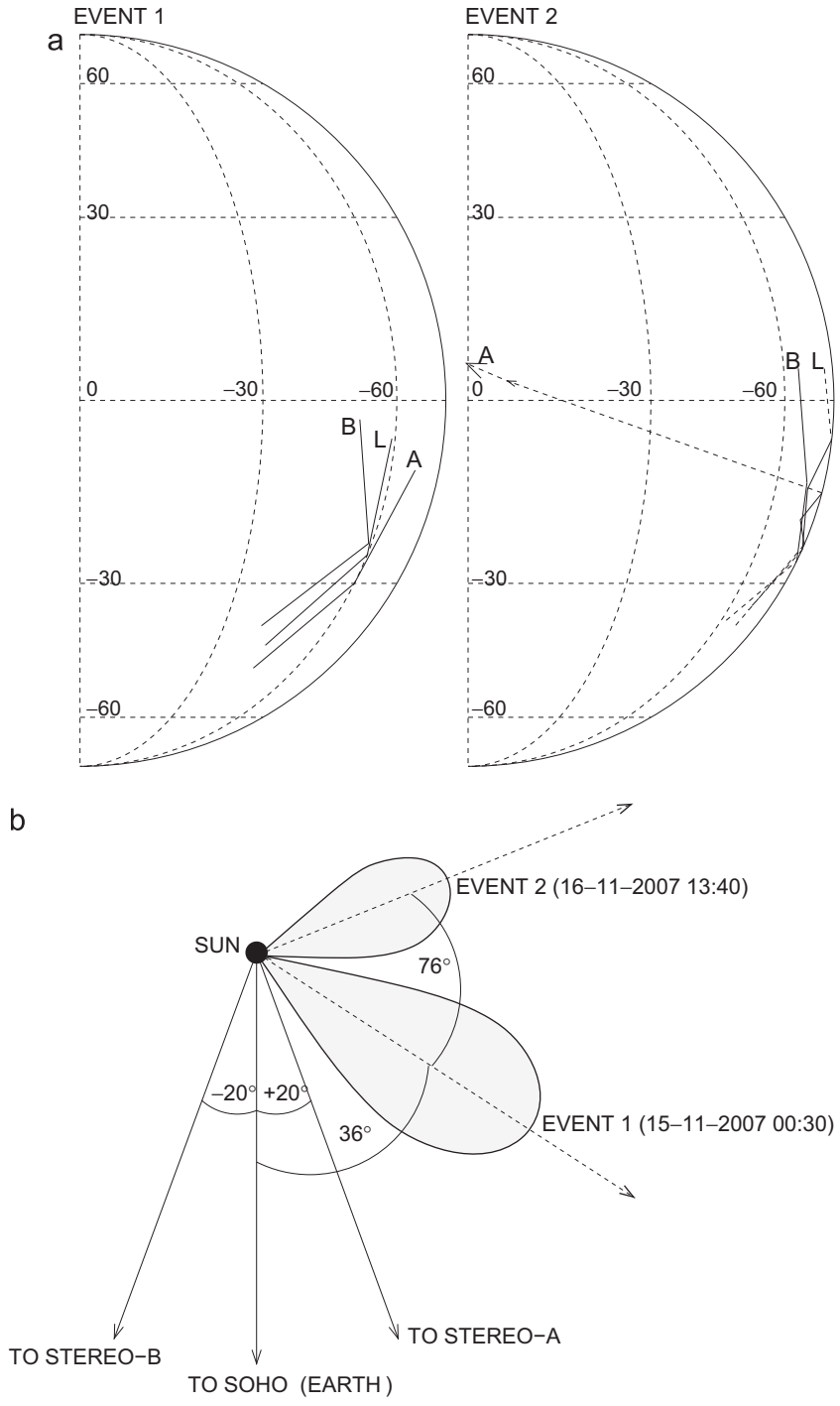

Fig. 2. The 3-D reconstruction of two CMEs reported by Howard and Tappin (2008). (a) Location on the solar surface of each event relative to LASCO (L), COR2-A (A) and COR2-A (B). (b) Ecliptic plane projection of both events at two different times. Event 2 is the event shown in Fig. 1. The Sun is at the center and the relative directions to the Earth and both STEREO are shown. The angular separation between Events 1 and 2 is 76° which is the separation between the two southern flanks.

the northern flank, central point and southern flank was 42°, 15°, and 76°, respectively, and the location of the southern flanks are shown in Fig. 2b. The difference in onset time between the two events was 40 h, during which time the Sun would have rotated around 23°.

Based on this, Howard and Tappin (2008) concluded that the CMEs probably originated from the same magnetic structure in the corona. A number of studies involving other techniques that take advantage of the stereoscopic capabilities of STEREO for CME reconstruction have since emerged and continue to do so, including forward modeling (e.g. Thernisien et al., 2006; Wood et al., 2009), tie-pointing (e.g. Mierla et al., 2009), inverse reconstruction (Antunes et al., 2009) and polarization ratio (Moran et al., 2010). Other triangulation efforts have also been made by (for example) de Koning et al. (2009), Liewer et al. (2009) and Temmer et al. (2009). Finally, efforts to more accurately define the masses of CMEs when observed in stereoscopic coronagraphs have developed, most notably by Colaninno and Vourlidas (2009). The review by Mierla et al. (2010) discusses many of these new and emerging techniques.

Please cite this article as: Howard, T.A., Three-dimensional reconstruction of coronal mass ejections using heliospheric imager.... Journal of Atmospheric and Solar-Terrestrial Physics (2010), doi:10.1016/j.jastp.2010.08.009

3. Heliospheric imagers

The need for stereoscopic views of CMEs in order to extract their 3-D properties can be overcome by imaging CMEs when they are at large distances from the Sun. This is because the linearity imposed on CMEs when they are close to the Sun breaks down when they are further away. One consequence of this breakdown is that we may no longer assume that we are observing the same point on a CME when measured from different viewpoints or even at different locations in the heliosphere.

While the linearity breakdown causes an increase in the complexity of the required CME analysis, it has the advantage that 3-D information can now be extracted from the images. Hence with a careful and detailed analysis of the geometry and scattering physics of the CME images we may extract some 3-D information from the images alone, without the need for auxiliary data or multiple viewpoints. To achieve this, we require an instrument capable of imaging CMEs when they are at large distances from the Sun and able to track them across very large distances through the heliosphere. Such an instrument is the heliospheric imager.

Heliospheric imagers work on a similar principal to coronagraphs, in that they observe CMEs in white light but at much further angular separations from the Sun. They are much more sensitive than coronagraphs, as they must observe CMEs to brightnesses down to 10^{-14} that of the Sun, but must also cover an intensity range spanning four orders of magnitude in order to accommodate the large change in apparent intensity of the CME (at a rate proportional to around r^{-4} where r is the distance from the Sun) as it evolves (Eyles et al., 2003). The first white light imager capable of observing CMEs at large distances was the E9 zodiacal light experiment on board the Helios spacecraft (Leinert et al., 1975), but the instrument had an extremely limited field of view. The first (almost) all-sky heliospheric imager was the Solar Mass Ejection Imager (SMEI), launched on board the Coriolis spacecraft in 2003 (Eyles et al., 2003). SMEI continues to operate to date and has detected and tracked well over 300 CMEs during its seven year lifespan. Studies of CMEs using SMEI include Tappin et al. (2004), Howard et al. (2006), Webb et al. (2006), Jackson et al. (2006, 2008), Howard and Simnett (2008), and Tappin and Howard (2009). The STEREO spacecraft, launched in 2006, carry the Heliospheric Imagers (HIs) that provide cleaner images of the heliosphere than SMEI, but with a field of view limited to around the ecliptic plane (Eyles et al., 2009). Studies of CMEs using the HIs include Harrison et al. (2008), Wood and Howard (2009), Davis et al. (2009) and Wang et al. (2009). Studies using both SMEI and the HIs include Webb et al. (2009) and Howard and Tappin (2009b, 2010).

4. Using heliospheric imagers to extract 3-D CME properties

Theoretically, the appearance of a CME in heliospheric imagers is a derivative of two coupled physical problems. These are the physics that enable us to observe the CME and the geometry of the structure as it moves relative to a fixed observer. The former involves the Thomson scattering of white light on the free electrons comprising the CME plasma while the latter requires knowledge of the overall structure of the CME and the application of physically and geometrically reasonable assumptions.

4.1. Thomson scattering: a brief review

The physics of Thomson scattering has been well established with theoretical investigations predating the discovery of the electron (Schuster, 1879). Further developments were made by Minnaert (1930) and a more rigorous treatment was applied by Billings (1966). The Billings treatment is the one that is commonly used for the analysis of CME densities today. A brief review of the theory of Thomson scattering, accommodating for large-distance scattering, follows.

When a plane electromagnetic wave of intensity I_0 is incident on a free electron, that electron will re-radiate in a pattern symmetrical about the direction of the incident wave. Following the treatment by Billings (1966) with modifications by Howard and Tappin (2009a), the total intensity of the scattered light I_{TOT} is given by

$$I_{TOT} = 2I_T - I_P, \tag{2}$$

where

$$I_T = I_0 \frac{\pi\sigma_e}{2z^2}[(1-u)C + uD], \tag{3}$$

and

$$I_P = I_0 \frac{\pi\sigma_e}{2z^2}\sin^2\chi[(1-u)A + uB]. \tag{4}$$

Here, σ_e is the differential cross section for perpendicular scattering,

$$\frac{e^4}{(4\pi\varepsilon_0)^2 m_e^2 c^4} \tag{5}$$

with e, m_e, ε_0 and c are the electron charge and mass, permittivity of free space and speed of light, respectively, z is the distance from the electron to the observer, u is the limb darkening coefficient and χ is the angle between the line of sight and the vector from the Sun through the scattering point. The parameters A, B, C and D are the so-called van de Hulst coefficients (named after van de Hulst, 1950 although they were actually formulated by Minnaert, 1930) and have the following form:

$$A = \cos\Omega \sin^2\Omega, \tag{6}$$

$$B = -\frac{1}{8}\left[1 - 3\sin^2\Omega - \frac{\cos^2\Omega}{\sin\Omega}(1+3\sin^2\Omega)\ln\left(\frac{1+\sin\Omega}{\cos\Omega}\right)\right], \tag{7}$$

$$C = \frac{4}{3} - \cos\Omega - \frac{\cos^3\Omega}{3}, \tag{8}$$

$$D = \frac{1}{8}\left[5 + \sin^2\Omega - \frac{\cos^2\Omega}{\sin\Omega}(5-\sin^2\Omega)\ln\left(\frac{1+\sin\Omega}{\cos\Omega}\right)\right]. \tag{9}$$

The van de Hulst coefficients are hence governed by a single independent variable Ω, where 2Ω is the apparent angular width of the Sun (i.e. the angular size of the Sun relative to the scattering point).

At large distances the Sun tends toward a point source, Ω becomes small and the van de Hulst coefficients tend towards $1/r^2$. The point of maximum scattering remains the point along each line of sight that is closest to the Sun, i.e. when $\chi = 90^\circ$. Close to the Sun this occurs in the plane of the sky but further away this is not the case. Vourlidas and Howard (2006) demonstrated that the locus of points satisfying $\chi = 90^\circ$ forms a sphere with the Sun-observer line as a diameter. They called it the "Thomson surface" and assuming that the CME was a single electron found that the distance of the electron from the Thomson surface dominated the determination of relative brightness of the CME. Howard and Tappin (2009a) showed that this is not because of the Thomson scattering itself (the scattering efficiency is actually minimized on the Thomson surface), but rather because the incident light and density along any line of sight are maximized here, and these parameters by far exceed the scattering efficiency. The combination of the three parameters results in a de-emphasis of the

Please cite this article as: Howard, T.A., Three-dimensional reconstruction of coronal mass ejections using heliospheric imager.... Journal of Atmospheric and Solar-Terrestrial Physics (2010), doi:10.1016/j.jastp.2010.08.009

importance of the Thomson surface, resulting in a spread of observed intensity to larger distances from the surface which is greater at larger distances from the Sun. This results in an increased reliability in mass calculations but at the cost of greater uncertainty in identification of the location of the observed electron(s). Mass calculations of CMEs using heliospheric imagers have been attempted by Jackson et al. (2006, 2007, 2008), and Bisi et al. (2008).

4.2. Geometry

Distances of points from the center of the Sun are actually in units of elongation ε, which is the angle between the Sun-observer line and the line of sight. In order to extract distance measurements from elongation, a number of assumptions must be applied. We have found that as elongation increases the required assumptions change. The next few sections review these assumptions and the elongation regions across which they are valid.

4.3. Elongations within 30°

The simplest conversion from elongation to distance applies when we are close to the Sun, i.e. within angles of around 15° ($\sim$0.25 AU or 55 $R_\odot$). Combining the Thomson scattering physics and geometry the following assumptions are applied:

1. The Point P approximation, which assumes the observed segment of the CME is a spherical arc, centered on the Sun (e.g. Houminer and Hewish, 1972; Howard et al., 2006). Point P requires $r = \sin\varepsilon$, where r is the distance from the Sun to the measured point.
2. Small angular separation from the Sun, so $\sin\varepsilon \sim \varepsilon$.

Hence, when CMEs are observed close to the Sun we may easily convert elongation to distance via the simple equation $r\,(\mathrm{AU}) = \varepsilon$ (rad). This approach, while significantly simplifying the conversion problem has the disadvantage of removing 3-D information from the image. Hence the necessary linearization of the geometry and scattering physics results in the exclusion of the ability to extract 3-D properties directly from white light CME images.

Beyond elongations of around 15°, the small angle assumption no longer applies but we may still apply the Point P approximation ($r = \sin\varepsilon$) to convert elongation to distance. Such a conversion was performed on measurements made in the early days of SMEI (e.g. Howard et al., 2006; Webb et al., 2006) and we have found that Point P is appropriate out to elongations of around 30°. This is equivalent to a distance of around 0.5 AU from the Sun.

4.4. Elongations between 30° and 45°

When CMEs are observed at elongations greater than around 30° Point P becomes less reliable. This is because the 3-D geometry of elongation as it relates to relative distance begins to become significant. Fig. 3 shows a range of elongation–time plots for a single point traveling at 1000 km/s and observed from the Earth (from Howard and Simnett, 2008, their Fig. 1a). In all cases the point is traveling in the ecliptic plane but the longitude of its direction of propagation is different. The differences in the elongation profiles are due to the motion of the point relative to the observer in each case. Taking the two extreme cases a point traveling at a longitude of 90° (i.e. in the plane of the sky) will take a very long time to reach the plane of the observer (at $\varepsilon = 90°$), so its elongation–time profile has a low gradient, reaching only 60°

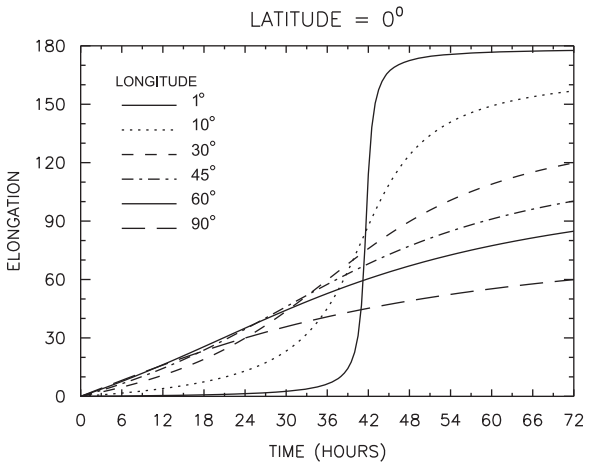

Fig. 3. Elongation vs. time plots for a single point moving through the heliosphere at 1000 km/s. In each case the point is in the ecliptic plane, the observer is at the Earth, and each plot represents the elongation–time plot for cases when the point is moving at different longitudes. The convention is such that 0° longitude represents a trajectory directly at the observer, so 90° indicates that the point is moving in the plane of the sky. Note that the elongation scale has a maximum of 180°, which is the point directly behind the observer when looking at the Sun (modified from Howard and Simnett, 2008).

after 72 h. The Earth-directed point, on the other hand, is not observed to change very much in elongation and then there is a sudden change as it passes the observer. We may visualise how a single point would appear to change in our field of view as it headed almost directly towards us. Note that in this case the point reaches the plane of the observer in just under 42 h after launch. This corresponds to the time a particle traveling at 1000 km/s would take to reach 1 AU (41 h, 40 min). This demonstrates the importance in the direction of propagation of the CME when converting elongation to distance. Also note that with the exception of those trajectories that are almost directly toward the observer (longitudes less than around 15°), there is a little difference between the elongation profiles within 30°.

The above consideration requires a 3-D geometrical treatment of CMEs when converting elongation to distance r. Howard et al. (2007) derived the following expression for this conversion, based on the geometry shown in Fig. 4 (modified from their Fig. 3):

$$\frac{1}{r} = \sin\alpha\cot\varepsilon + \cos\alpha, \tag{10}$$

where α is the angle subtended by Q at the Sun. It can readily be shown that

$$\cos\alpha = \sin\theta\cos\phi, \tag{11}$$

where θ and ϕ are the co-latitude and longitude.

This results in the following expressions for the 3-D speed and acceleration (Howard et al., 2008):

$$v_{3D} = \frac{dr}{dt} = r^2\sin\alpha\,\mathrm{cosec}^2\,\varepsilon\frac{d\varepsilon}{dt}, \tag{12}$$

and

$$a_{3D} = \frac{d^2r}{dt^2} = \frac{v_{3D}}{d\varepsilon/dt}\left(\frac{d^2\varepsilon}{dt^2}\right) + 2v_{3D}\left[\frac{v_{3D}}{r} - \cot\varepsilon\left(\frac{d\varepsilon}{dt}\right)\right], \tag{13}$$

where

$$\frac{d\varepsilon}{dt} = v_0\sec\varepsilon, \tag{14}$$

and

$$\frac{d^2\varepsilon}{dt^2} = a_0\sec\varepsilon + V_0^2\tan\varepsilon\sec^2\varepsilon. \tag{15}$$

Please cite this article as: Howard, T.A., Three-dimensional reconstruction of coronal mass ejections using heliospheric imager.... Journal of Atmospheric and Solar-Terrestrial Physics (2010), doi:10.1016/j.jastp.2010.08.009

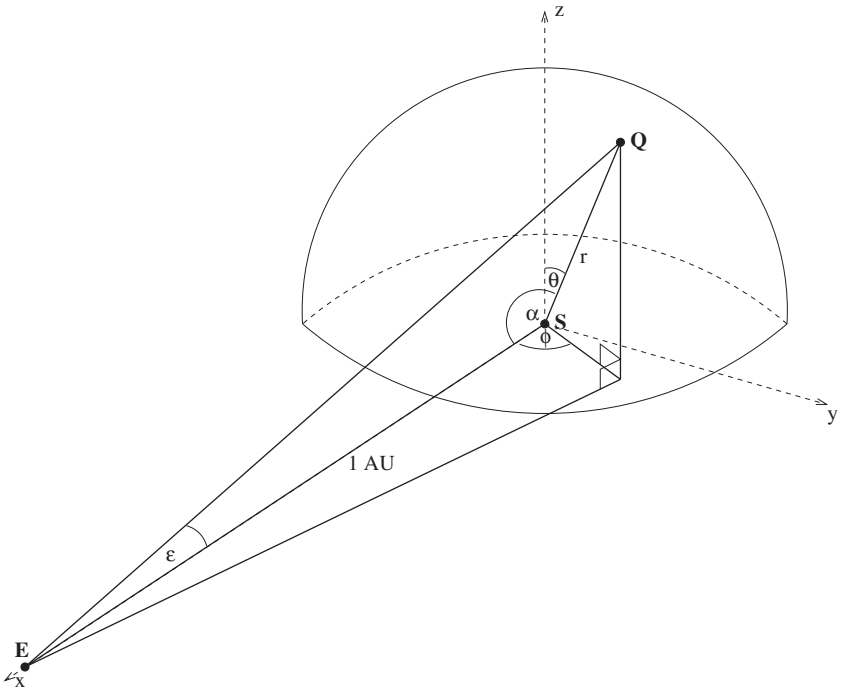

Fig. 4. Geometry of a single point observed in an arbitrary point in 3-D space. The point Q has spherical coordinates (r,θ,ϕ) and the observer at the Earth E is also indicated. Two further angles are shown, the elongation ε and the angle subtended by the point at the Sun α. This figure enables the geometrical relationship between r and ε to be determined (modified from Howard et al., 2007).

Here v_0 and a_0 are the sky-plane projected speed and acceleration, respectively.

This method of conversion of elongation to distance is now known as the Fixed-Phi Method (Sheeley et al., 1999; Kahler and Webb, 2007) and requires information on the direction of the CME (i.e. θ and ϕ) for utility. Previous studies using this technique have obtained these from auxiliary datasets (Howard et al., 2007; Kahler and Webb, 2007; Webb et al., 2009). Howard and Simnett (2008) attempted to extract them using a data cube of simulated elongation–time curves which were compared with those measured directly from SMEI CME datasets. This was met with mixed success, probably because Fixed-Phi only seems to be appropriate out to elongations around 45° (~0.7 AU).

4.5. Elongations beyond 45°

Once the CME moves beyond elongations around 45° not only does the direction of propagation play a role but also the structure of the CME itself. This is because distances are generally determined using the leading edge of the CME, which is the point on the structure that makes a tangent with the line of sight. Close to the Sun it may be safely assumed that leading edge measurements of a CME in successive images are at the same point on the CME structure, but far from the Sun this assumption is no longer valid.

Variations in distance calculations derived from the Fixed-Phi method have appeared in measurements derived from SMEI images at large elongations but these have not been published. We found that at large elongations there is a sudden apparent increase in the speed of the CME. This is not a real effect, but rather the result of the changing location of the apparent leading edge. A demonstration of this effect is shown in Fig. 5, which is for the oversimplified case of an expanding spherical bubble. Panel a shows the location of the CME when the original measurement is made, with the circle and cross overlaying. As the CME expands in panels b and c the actual measured leading edge is indicated by the crosses while the circles indicate the location of the original measured point on the CME. This demonstrates that if we were to assume that the same location is observed each time, then distance derivations from the leading edge would appear to be further from the Sun than it actually was, with the difference between apparent and actual locations increasing as the CME expands (Howard and Tappin, 2009a).

This simple demonstration shows how the relative geometry of the CME plays an important role when it is at large distances from the Sun. To overcome this problem we must combine the structure of the CME with the physics that allow us to observe it. Complex treatments of these two problems have been performed by a number of workers, including Odstrcil et al. (2003) and Jackson et al. (2008), but much can be achieved with basic assumptions of CME leading edge structure without requiring assumptions of the physics of CME evolution. One popular base structure is known as the cone model (Zhao et al., 2002; Zhao, 2008) which assumes the CME is a spherical shell with the Sun at the center, while other workers (e.g. Lugaz et al., 2009) have assumed the CME takes the form of a spherical bubble with the Sun at one point on the circumference. Howard and Tappin (2009a) showed that the spherical bubble case may be described in terms of the distance of the assumed point from the Sun r, the difference between the assumed and actual distance δr and the angle between the Sun–Earth line and the diameter of the CME sphere λ:

$$r+\delta r=\frac{r}{2}(1+\mathrm{cosec}(\lambda+\varepsilon)), \tag{16}$$

or

$$r=\frac{2R_0\sin\varepsilon\,\mathrm{cosec}(\lambda+\varepsilon)}{1+\mathrm{cosec}(\lambda+\varepsilon)}, \tag{17}$$

where R_0 is the distance from the observer to the Sun. It should be obvious that $r+\delta r$ is the actual distance of the measured point

Please cite this article as: Howard, T.A., Three-dimensional reconstruction of coronal mass ejections using heliospheric imager.... Journal of Atmospheric and Solar-Terrestrial Physics (2010), doi:10.1016/j.jastp.2010.08.009

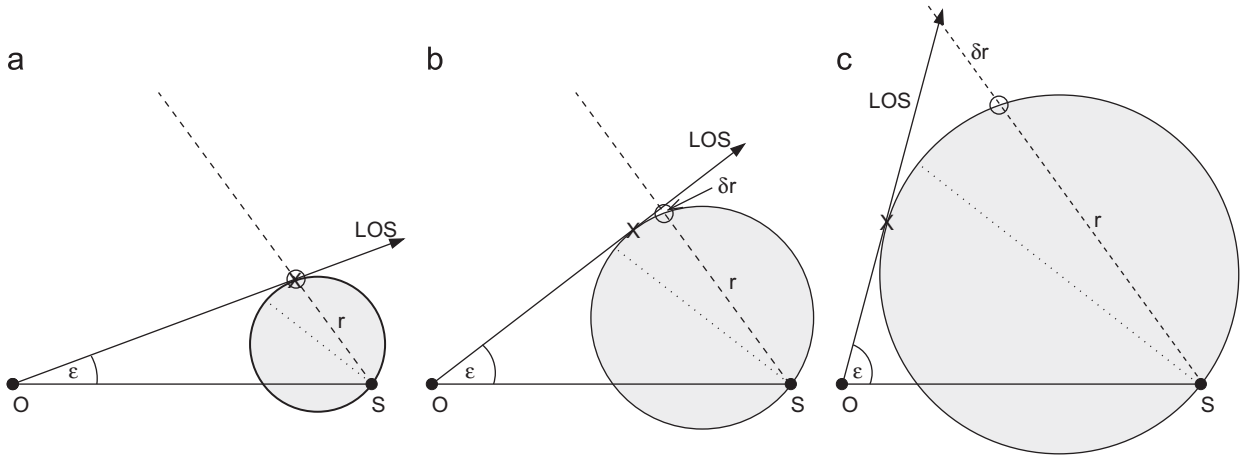

Fig. 5. A demonstration of the effects of CME structure across large distances (elongations). This is for the oversimplied case of a CME as a perfect sphere (bubble). In each case the circle represents the location of the original measurement of the leading edge and the point on the CME where we would typically assume all leading measurements are located. The crosses are the actual location of the leading edge, and LOS is the line of sight. The dotted line is the diameter in each case. Close to the Sun (a) the first measurement is made and the circle and cross overlay, but further away (b) the leading edge is no longer at the same place. This leads to an overestimation of the true location of the CME. This separation becomes greatly exaggerated when the CME is close to the observer (c).

from the Sun. For the spherical shell, Howard and Tappin (2009a) found that there were three geometrical cases to consider since the shell was not continuous across all space. Hence the three cases were those where the line of sight was tangent to the shell, and the two cases when it passed through the two edges of the shell, denoted E_1 and E_2. The conversion of ε to r may be achieved by considering each case separately. That is,

$$r = R_0 \sin\varepsilon \quad \text{when the LOS is a tangent to the front, i.e. } 90^\circ - (\lambda + \delta\lambda) < \varepsilon < 90^\circ - (\lambda - \delta\lambda),$$

$$r = R_0 \sin\varepsilon : \operatorname{cosec}(\varepsilon + (\lambda - \delta\lambda)) \quad \text{when the LOS contacts at } E_1, \text{ i.e. } \varepsilon > 90^\circ - (\lambda - \delta\lambda),$$

$$r = R_0 \sin\varepsilon \operatorname{cosec}(\varepsilon + (\lambda + \delta\lambda)) \quad \text{when the LOS contacts at } E_2, \text{ i.e. } \varepsilon < 90^\circ - (\lambda + \delta\lambda), \tag{18}$$

where $\delta\lambda$ is half the angular width of the shell or the angle from the central axis to its edge. E_1 and E_2 represent the inner and outer edges of the shell relative to the observer (refer to Fig. 10e of Howard and Tappin, 2009a).

4.6. Extracting 3-D parameters

The above analysis shows that when the CME is at sufficiently large distances from the Sun, then 3-D information about its direction of propagation (when $\varepsilon > 30^\circ$) and structure (when $\varepsilon > 45^\circ$) may be extracted from white light images alone. Tappin and Howard (2009) demonstrated one method by which this may be achieved by comparing apparent leading edges simulated from the two basic structures with actual leading edges measured from heliospheric images of CMEs. This technique, that we call the Tappin–Howard (TH) Model, constructs the leading edges from a combination of parameters describing the structure and kinematics of the simulated CME. These parameters are central latitude and longitude, latitude and longitude width, distance, speed and distortion, and each parameter is allowed to vary to construct a unique leading edge in each case. When the collective of leading edges is compared with those actually measured from the heliospheric dataset the combination of parameters best matching the measured leading edges is determined, along with a measurement of the "goodness" of fit of each parameter. Those parameters can then be used to estimate the structure and kinematic evolution of the CME.

The purpose of the TH Model is to provide a high-speed estimate of the leading edge of the CME. It does not attempt to reproduce the density structure and cannot extract finer structures within the leading edge. It is designed to convert elongation to distance and provide an estimate of the overall structure of the leading edge of the CME, and so can estimate kinematic evolution and arrival time, speed and impact probability at the Earth. It is limited by the base structure and gradient of the converging parameters, and so can be regarded as a high-speed reconstruction tool. We have found that certain parameters converge more reliably than others depending on the CME being measured. For example, a limb CME has a poorly constrained longitude width parameter because a large range of longitude widths can be assigned to a CME without significantly changing the structure of its apparent leading edge. To provide a measurement of the reliability of convergence of parameters we provide error plots such as those in Tappin and Howard (2009, Figures 7, 9, 11, 13, 15).

The reliability of TH has been tested on a number of case studies (Tappin and Howard, 2009; Howard and Tappin, 2009b, 2010) with regard to impact probability and arrival time and speed, with results we regard as a promising improvement to existing forecasting techniques. Further studies of the model are required before a proper evaluation of its performance can be conducted, and a validation and statistical survey of a large number of CMEs is currently underway.

5. The results from one method of 3-D parameter extraction

There are a number of advantages of using heliospheric image data to identify 3-D parameters of CMEs. The strongest is the dependence on a single dataset—the heliospheric imager itself. Leading edge comparison techniques such as the TH Model have the added advantage of high speed of operation. They also do not require any assumptions of the evolutionary nature of the CME, thus removing a potential source of uncertainty. The potential accuracy of the model has been demonstrated in a number of papers, including Tappin and Howard (2009) and Howard and

Please cite this article as: Howard, T.A., Three-dimensional reconstruction of coronal mass ejections using heliospheric imager.... Journal of Atmospheric and Solar-Terrestrial Physics (2010), doi:10.1016/j.jastp.2010.08.009

Tappin (2009b, 2010). Here we discuss the results from a single event discussed by Tappin and Howard (2009).

5.1. The event

The CME was Earth-directed and detected by the LASCO coronagraph (Brueckner et al., 1995), the SMEI heliospheric imager (Eyles et al., 2003) and the in situ ACE and WIND spacecraft. It was part of a group of four events that were observed over the same time period. Careful evaluation of these has revealed that they are four separate structures and not part of the same CME. Converged parameters using TH were very different for each event, which would seem to agree with this assessment (note that we have identified other multiple structures in other events that have produced very similar parameters in TH which has led us to believe they were parts of the same CME). The event we present here was the earliest and brightest of the four events. Associated phenomena were also detected by solar X-ray and EUV imagers and by ground-based magnetometers. It first appeared in LASCO at 00:26 UT on 3 December 2004 and in SMEI at around 06:00 UT on 4 December. There was an associated X-ray flare at 00:00 UT on 3 December and a post-eruptive arcade and coronal dimming were observed by the EIT EUV solar imager. ACE at the L1 lagrange point detected a shock at 06:56 UT on 5 December, WIND near the Earth detected it at 07:04 UT, and a small geomagnetic storm occurred at Earth on 6 December. Fig. 6 shows the EIT, LASCO and SMEI images of the event and Fig. 7 shows the ACE and WIND magnetic field and solar wind plasma data. Note that there was an earlier enhancement (probably a weak shock) at 04:10 UT (ACE) and 04:31 UT (WIND) on the same day, but this is probably associated with one of the other three events. In Fig. 6 three of the four events can be seen, indicated by the arrows. The event closest to the Sun to the north of the image is the event we present here.

5.2. Three-dimensional parameters

Table 1 shows the converging parameters for the entire data set, i.e. with the combination of leading edges measured in the SMEI data for the duration of the event. Tappin and Howard (2009) performed separate TH model convergences on each of the four structures observed in the SMEI dataset, and we show here the fitting for the selected event. This describes the direction, size, speed and structure of the leading edge of the CME, as determined by TH, and Fig. 8 shows one image of the 3-D structure from these parameters at 16:48 UT on 4 December, from Fig. 10f of Tappin and Howard (2009).

The TH Model also operates in a second stage where any parameter can be made to vary while others remain fixed in their Stage One values. We vary speed, but could choose to vary direction, size, or in the later version of the model, base structure (Howard and Tappin, 2010). Varying speed enables a description of the kinematic evolution of the CME as it moves through the heliosphere, but fixes the size and direction parameters. This is therefore based on the assumption that the angular size, structure and direction of the CME do not change in transit, with all the disadvantages incurred with such an assumption. Fig. 9 shows the resulting 3-D height-time plot of the CME derived from the model (Fig. 10c of Tappin and Howard, 2009). For comparison, the LASCO height-time data and the time of the arrival of the interplanetary

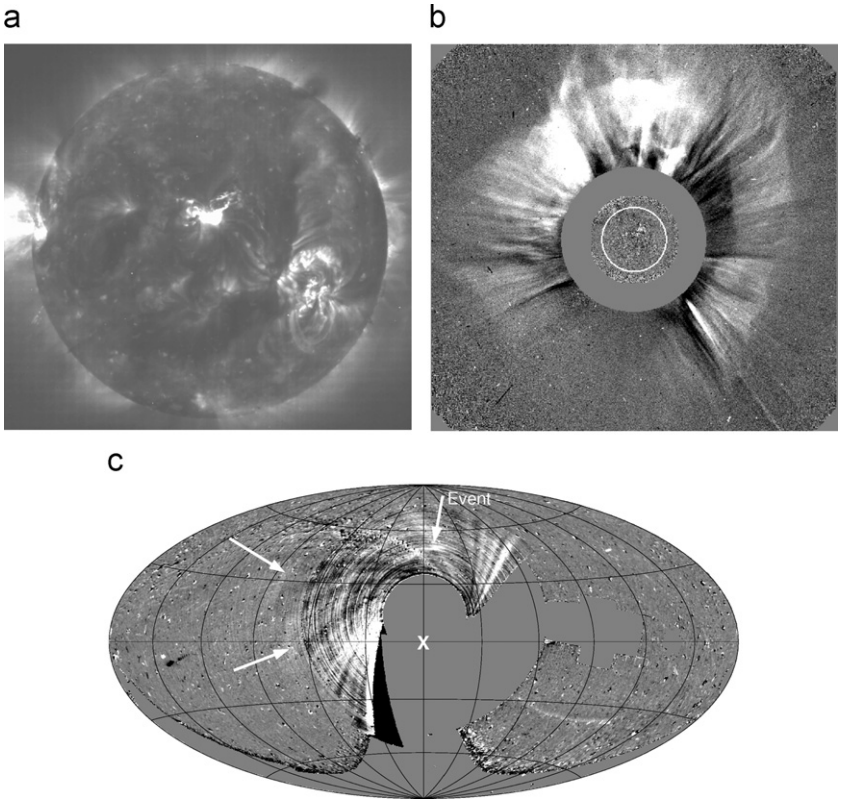

Fig. 6. (a) EIT, (b) LASCO, and (c) SMEI images of the Earth-directed CME first observed around 00:00 UT on 3 December 2004. The EIT image was obtained at 00:00 UT and the LASCO C2 image at 00:50 UT on 3 December (obtained from the CDAW CME Catalog). The SMEI image was obtained between 15:57 and 17:39 UT on 4 December. In the LASCO image the white circle indicates the solar disk while the Sun is located by the white cross in the SMEI image. The arrows indicate three of the four separate events observed during this time period, and the brightest event (labeled "Event") to the north is the one we present here.

Please cite this article as: Howard, T.A., Three-dimensional reconstruction of coronal mass ejections using heliospheric imager.... Journal of Atmospheric and Solar-Terrestrial Physics (2010), doi:10.1016/j.jastp.2010.08.009

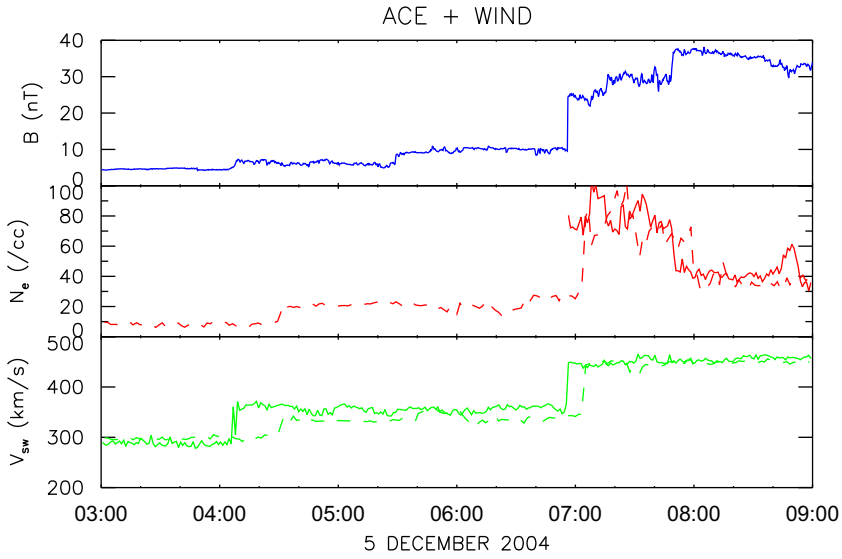

Fig. 7. In situ ACE (solid) and WIND (dashed) magnetic field (blue), solar wind density (red) and solar wind speed (green) plots for a 6 h time period from 03:00 to 09:00 UT on 5 December 2004. ACE/SWEPAM density data are missing up until 06:57 and WIND/MFI data are missing for the entire time period. This shows the arrival of a strong forward shock at ACE at 06:56 UT and at WIND at 07:04 UT, and a likely weak shock at ACE at 04:10 UT and at WIND at 04:31 UT. We believe the event observed here is associated with the strong shock. (For interpretation of the references to color in this figure legend, the reader is referred to the web version of this article.)

Table 1
Converging parameters for the TH Model run on the brightest component of the event.

Parameter	Value
Base structure	Shell
Starting height	0.57 AU
Speed	657 km/s
Central latitude	39°N
Central longitude	6°E
Latitude width	27°
Longitude width	39°

It was found that a spherical shell best fit the dataset.

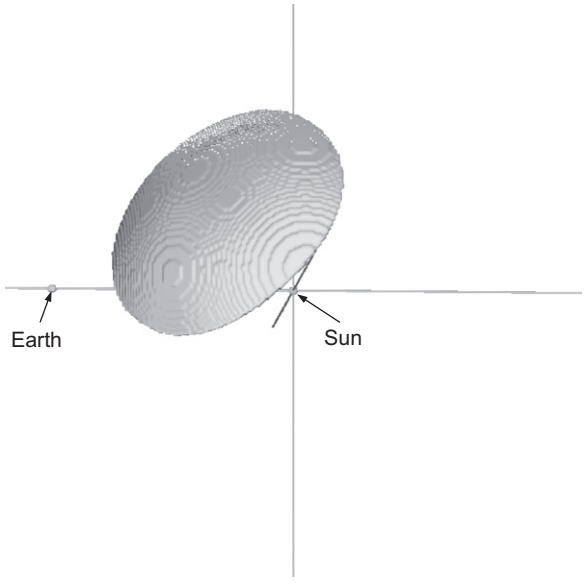

Fig. 8. Three-dimensional reconstruction of the event from the parameters derived in the TH Model at 16:48 UT on 4 December 2004 (Tappin and Howard, 2009). The location of the Sun and Earth are indicated and the perspective is from the direction of the Ulysses spacecraft at this time. Note that the Earth lies to one flank of this 3-D structure.

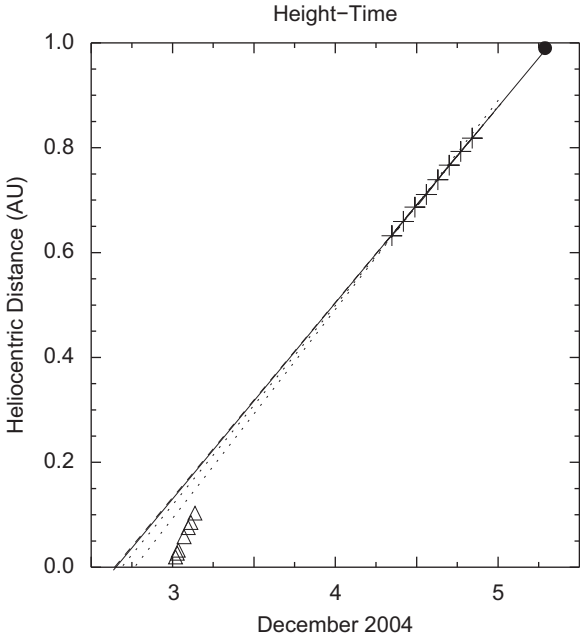

Fig. 9. Three-dimensional height-time plot of the TH Model reconstruction of the event. The LASCO height-time data and the time of the arrival of the shock at ACE have also been included. The SMEI data are projected backward to estimate its launch time (line), and forward to predict its arrival time at the Earth (modified from Tappin and Howard, 2009). The triangles represent the LASCO data, the black circle is the arrival time of the shock at ACE, and the pluses indicate the 3-D distance as determined by TH.

shock as detected by the ACE spacecraft have been included. As shown in this plot the speed for this particular CME is relatively constant, and we may project its trajectory both backward to identify the timing of the launch and forward to predict the arrival time at ACE. It is not difficult to match the dataset with the LASCO halo CME if we assume that a deceleration has occurred between LASCO and SMEI. This is reasonable given that the LASCO event has a speed of around 1100 km/s but in SMEI the speed is around 660 km/s. We note that the bulk plasma speed as shown in Fig. 7

Please cite this article as: Howard, T.A., Three-dimensional reconstruction of coronal mass ejections using heliospheric imager.... Journal of Atmospheric and Solar-Terrestrial Physics (2010), doi:10.1016/j.jastp.2010.08.009

is around 450 km/s, while TH predicts a speed of 660 km/s. While one may expect the shock to travel faster than the bulk speed (e.g. Howard and Tappin, 2005) we would not expect an increase by this quantity. Even if we assume the material observed by SMEI is built-up shocked material rather than the CME itself, the speed of that shock is only around 500 km/s. Hence the TH Model has over-estimated the speed of this CME by around 150 km/s.

When we project the height-time dataset forward we predict an arrival time at ACE of 07:15 UT on 5 December, which in this case is 19 min later than its actual arrival. It is therefore possible to achieve arrival time predictions with a high degree of accuracy by simply analyzing heliospheric images and applying geometry and Thomson scattering principles.

5.3. Evolving accuracy

In order to monitor the accuracy of the TH Model, Howard and Tappin (2010) conducted mock space weather forecasts, where they ran the TH Model and predicted the time of arrival as each new SMEI image became available. The results for the event discussed here are shown in Fig. 10 (Howard and Tappin, 2010, their Fig 6b). As the Model could be run a number of times during the latency of SMEI we show the median predicted arrival times as well as the largest and smallest times. The horizontal line represents the time of arrival at ACE as does the asterisk, so the closer the data points are to the asterisk in the *x*-direction the later the time at which the prediction was made, and the closer the points are to the horizontal line in the *y*-direction the more accurate the prediction.

As shown in Fig. 10, for this event the early predictions were relatively inaccurate (off by around 10 h) but this accuracy improved with passing time. Accuracies within an hour were obtained 5 h before impact and the last forecast, made 2 h before impact, was 19 min off. Further studies on other events have been conducted with varying, yet encouraging, degrees of accuracy. A validation and statistical survey is currently underway.

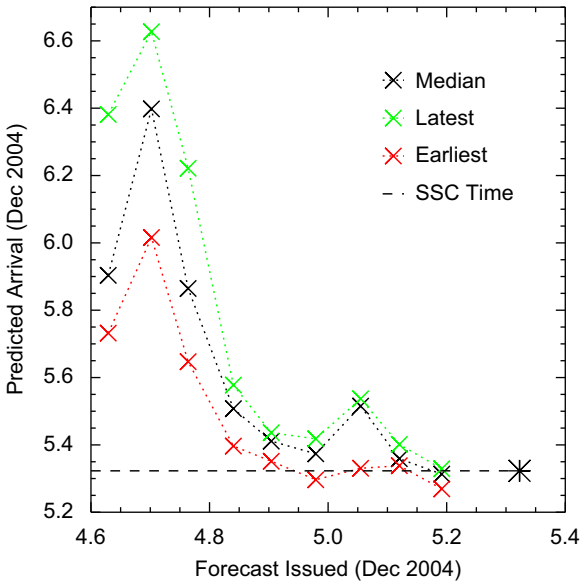

Fig. 10. Predicted arrival time vs. time of forecast for the event reported by Howard and Tappin (2010) and obtained by running the TH Model a number of times. The middle plot represents the median forecast arrival time while the upper and lower plots are the maximum and minimum forecast times, respectively. The asterisk and horizontal line represents the time of the storm onset, so the closer the points are to the asterisk the later the prediction was issued and the closer to the horizontal line the more accurate the prediction.

6. Summary and conclusions

Extraction of three-dimensional properties from CMEs have been elusive since their discovery in the 1970s. This is because of the linear nature of the geometry combined with the Thomson scattering physics that allow us to observe the CME in white light. This results in coronagraph images that are projected into the sky plane.

The STEREO spacecraft provide an unprecented ability to obtain a 3-D picture of CMEs from the coronagraph data alone. This is by means of geometrical triangulation assuming that a measured point from multiple viewpoints is the same physical point in 3-D space—a safe assumption when observing relatively close to the Sun. Such a practice has been conducted by many workers and has achieved great success at obtaining 3-D CME parameters. This represents a major milestone in CME study and in coronagraph analysis.

It has been demonstrated that another white light instrument is available that can be used to obtain 3-D CME properties without the need for multiple viewpoints or auxiliary data. This is the heliospheric imager that observes CMEs at very large distances from the Sun. It has been shown that as the CME is imaged at larger distances the linearity simplifying (and restricting) the analysis of CMEs close to the Sun breaks down. This requires a more complex treatment but enables the extraction of 3-D properties.

The level of complexity in CME analysis in heliospheric imagers varies, but it has been shown that relatively simple analyses can describe the structure and kinematic evolution of CMEs with a reasonable degree of accuracy. The potential for scientific advancement of our understanding of CMEs and for space weather forecasting has been demonstrated.

6.1. Concluding remarks

The author hopes that the importance of heliosperic imaging for CME and space weather study has been made clear in this review of the most recent advances in these areas carried out by the author and colleagues. With this in mind, it is important to note that the heliospheric imagers currently operating will soon be reaching the end of their usable life, or more specifically the end of their useful life for space weather study and forecasting.

The current heliospheric imagers are SMEI on board Coriolis and the Heliospheric Imagers (HIs) on STEREO. SMEI has been in operation since early 2003 and its innermost camera (Camera 3) has been suffering an accumulative hot pixel degradation during its lifetime. This has reached the point where Camera 3 is virtually useless for CME detection and will be completely so in the next year or two. Without Camera 3, CMEs will not be observed by SMEI until they arrive in its Camera 2, when they are around 0.7 AU from the Sun. The STEREO spacecraft continue to increase their angular separation on their orbit about the Sun and will reach the solar plane towards the end of 2011. Beyond this point CMEs directed toward the Earth will be backsided relative to STEREO and no heliospheric imager has ever observed a backsided CME (because of the large distance of backsided CMEs from the observer and its Thomson surface).

Hence by around the end of 2011 no heliospheric imager will be available that can observe Earth-directed CMEs for almost all of their journey to the Earth, and no replacement imager is currently underway. This means that we risk losing the advancements made with heliospheric imagers in the areas of space weather study and forecasting. It is the author's hope that support in the community will lead to the development of a next generation heliospheric imager, so that further advancements can be

Please cite this article as: Howard, T.A., Three-dimensional reconstruction of coronal mass ejections using heliospheric imager.... Journal of Atmospheric and Solar-Terrestrial Physics (2010), doi:10.1016/j.jastp.2010.08.009

accomplished and the full capability of this unique class of instrument realized.

References

Andrews, M.D., Howard, R.A., Michels, R.A., Lamy, P.L., Schwenn, R., Simnett, G.M., 1998. The visibility of "Halo" coronal mass ejections. Phys. Chem. Earth 24, 57.

Antunes, A., Thernisien, A., Yahil, A., 2009. Hybrid reconstruction to derive 3D height-time evolution for coronal mass ejections. Solar Phys. 259, 199.

Baker, D.N., Balstad, R., Bodeau, J.M., Cameron, E., Fennel, J.F., Fisher, G.M., Forbes, K.F., Kintner, P.L., Leffler, L.G., Lewis, W.S., Reagan, J.B., Small III, A.A., Stansell, T.A., Strachan Jr., L., 2009. Severe Space Weather Events—Understanding Societal and Economic Impacts: A Workshop Report. The National Academies Press, Washington, DC.

Billings, D.E., 1966. A Guide to the Solar Corona. Academic Press, New York.

Bisi, M.M., Jackson, B.V., Hick, P.P., Buffington, A., Odstrcil, D., Clover, J.M., 2008. Three-dimensional reconstructions of the early November 2004 Coordinated Data Analysis Workshop geomagnetic storms: analyses of STELab IPS speed and SMEI density data. J. Geophys. Res. 113, A00A11. doi:10.1029/2008JA013222.

Brueckner, G.E., Howard, R.A., Koomen, M.J., Korendyke, C.M., Michels, D.J., Moses, J.D., Socker, D.G., Dere, K.P., Lamy, P.L., Llebaria, A., Bout, M.V., Schwenn, R., Simnett, G.M., Bedford, D.K., Eyles, C.J., 1995. The large angle spectroscopic coronagraph. Solar Phys. 162, 357.

Colaninno, R.C., Vourlidas, A., 2009. First determination of the true mass of coronal mass ejections: a novel approach to using the two STEREO viewpoints. Astrophys. J. 698, 852.

Davis, C.J., Davies, J.A., Lockwood, M., Rouillard, A.P., Eyles, C.J., Harrison, R.A., 2009. Stereoscopic imaging of an earth-impacting solar coronal mass ejection: a major milestone for the STEREO mission. Geophys. Res. Lett. 36, L08102. doi:10.1029/2009GL038021.

de Koning, C.A., Pizzo, V.J., Biesecker, D.A., 2009. Geometric localization of CMEs in 3D space using STEREO beacon data: first results. Solar Phys. 256, 167.

Dungey, J.W., 1961. Interplanetary magnetic field and the aurora. Phys. Rev. Lett. 6, 47.

Dungey, J.W., 1963. In: DeWitt, C., Hieblot, J., Lebeau, A. (Eds.), Geophysics: The Earth's Environment. Gordon Breach, New York.

Emslie, A.G., Kucharek, H., Dennis, B.R., Gopalswamy, N., Holman, G.D., Share, G.H., Vourlidas, A., Forbes, T.G., Gallagher, P.T., Mason, G.M., Metcalf, T.R., Metwaldt, R.A., Murphy, R.J., Schwartz, R.A., Zurbuchen, T.H., 2004. Energy partition in two flare/CME events. J. Geophys. Res. 109, A10104. doi:10.1029/2004JA010571.

Eyles, C.J., Simnett, G.M., Cooke, M.P., Jackson, B.V., Buffington, A., Hick, P.P., Waltham, N.R., King, J.M., Anderson, P.A., Holladay, P.E., 2003. The Solar Mass Ejection Imager (SMEI). Solar Phys. 217, 319.

Eyles, C.J., Harrison, R.A., Davis, C.J., Waltham, N.R., Shaughnessy, B.M., Mapson-Menard, H.C.A., Bewsher, D., Crothers, S.R., Davies, J.A., Simnett, G.M., Howard, R.A., Moses, J.D., Newmark, J.S., Socker, D.G., Halain, J.-P., Defise, J.-M., Mazy, E., Rochus, P., 2009. The heliospheric imagers onboard the STEREO mission. Solar Phys. 254, 387.

Falconer, D.A., Moore, R.L., Gary, G.A., 2002. Correlation of the coronal mass ejection productivity of solar active regions with measures of their global nonpotentiality from vector magnetograms: baseline results. Astrophys. J. 569, 1016.

Gopalswamy, N., 2009. CME link to the geomagnetic storms 2009. In: Andrei, A.H., Kosovichev, A., Rozelot, J.-P. (Eds.), Proceedings of the IAU Symposium, vol. 264, p. 119.

Gopalswamy, N., 2004. The sun and the heliosphere as an integrated system. In: Poletto, G., Suess, S.T. (Eds.), Astrophysics and Space Science Library. Kluwer, Dordrecht, pp. 204.

Gopalswamy, N., Akiyama, S., Yashiro, S., Michalek, G., Lepping, R.P., 2007. Solar sources and geospace consequences of interplanetary magnetic clouds observed during solar cycle 23. J. Atmos. Solar-Terr. Phys. 70, 245.

Gosling, J.T., 1993. The solar flare myth. J. Geophys. Res. 98, 18937.

Gosling, J.T., Hildner, E., MacQueen, R.M., Munro, R.H., Poland, A.I., Ross, C.L., 1974. Mass ejections from the Sun—a view from SKYLAB. J. Geophys. Res. 79, 4581.

Harrison, R.A., Davis, C.J., Eyles, C.J., Bewsher, D., Crothers, S.R., Davies, J.A., Howard, R.A., Moses, D.J., Socker, D.G., Newmark, J.S., Halain, J-P., Defise, J-M., Mazy, E., Rochus, P., Webb, D.F., Simnett, G.M., 2008. First imaging of coronal mass ejections in the heliosphere viewed from outside the sun earth line. Solar Phys. 247, 171.

Harrison, R.A., Waggett, P.W., Bentley, R.D., Phillips, K.J.H., Bruner, M., Dryer, M., Simnett, G.M., 1985. The X-ray signature of solar coronal mass. Solar Phys. 97, 387.

Houminer, Z., Hewish, A., 1972. Long-lived sectors of enhanced density irregularities in the solar wind. Planet. Space Sci. 20, 1703.

Howard, R.A., Moses, J.D., Vourlidas, A., Newmark, J.S., Socker, D.G., Plunkett, S.P., Korendyke, C.M., Cook, J.W., Hurley, A., Davila, J.M., Thompson, W.T., St. Cyr, O.C., Mentzell, E., Mehalick, K., Lemen, J.R., Wuelser, J.P., Duncan, D.W., Tarbell, T.D., Wolfson, C.J., Moore, A., Harrison, R.A., Waltham, N.R., Lang, J., Davis, C.J., Eyles, C.J., Mapson-Menard, H., Simnett, G.M., Halain, J.-P., Defise, J.-P., Mazy, E., Rochus, P., Mercier, R., Ravet, M.F., Delmotte, F., Auchere, F., Delaboudiniére, J.-P., Bothmer, V., Deutsch, W., Wang, D., Rich, N., Cooper, S., Stephens, V., Maahs, G., Baugh, R., McMullin, D., 2008. Sun-Earth connection coronal and heliospheric investigation (SECCHI). Space Sc. Rev. 136, 67.

Howard, T.A., Fry, C.D., Johnston, J.C., Webb, D.F., 2007. On the evolution of coronal mass ejections in the interplanetary medium. Astrophys. J. 667, 610.

Howard, T.A., Nandy, D., Koepke, A.C., 2008. Kinematic properties of solar coronal mass ejections: correction for projection effects in spacecraft coronagraph measurements. J. Geophys. Res. 113, A01104. doi:10.1029/2007JA012500.

Howard, T.A., Simnett, G.M., 2008. Interplanetary coronal mass ejections that are undetected by solar coronagraphs. J. Geophys. Res. 113, A08102. doi:10.1029/2007JA012920.

Howard, T.A., Tappin, S.J., 2005. Statistical survey of earthbound interplanetary shocks, associated coronal mass ejections and their space weather consequences. Astron. Astrophys. 440, 373.

Howard, T.A., Tappin, S.J., 2008. Three-dimensional reconstruction of two solar coronal mass ejections using the STEREO spacecraft. Solar Phys. 252, 373.

Howard, T.A., Tappin, S.J., 2009a. Interplanetary coronal mass ejections observed in the heliosphere: 1. Review of Theory. Space Sci. Rev. 147, 31.

Howard, T.A., Tappin, S.J., 2009b. Interplanetary coronal mass ejections observed in the heliosphere: 3. Physical implications. Space Sci. Rev. 147, 89.

Howard, T.A., Tappin, S.J., 2010. The application of a new phenomenological coronal mass ejection model to space weather forecasting, Space Weather 8, S07004. doi:10.1029/2009SW000531.

Howard, T.A., Webb, D.F., Tappin, S.J., Mizuno, D.R., Johnston, J.C., 2006. Tracking halo coronal mass ejections from 0–1 AU and space weather forecasting using the solar mass ejection imager (SMEI). J. Geophys. Res. 111, A04105. doi:10.1029/2005JA011349.

Hundhausen, A.J., Burkepile, J.T., St. Cyr, O.C., 1994. Speeds of coronal mass ejections: SMM observations from 1980 and 1984–1989. J. Geophys. Res. 99, 6543.

Jackson, B.V., Bisi, M.M., Hick, P.P., Buffington, A., Clover, J.M., Sun, W., 2008. Solar mass ejection imager 3-D reconstruction of the 27–28 May 2003 coronal mass ejection sequence. J. Geophys. Res. 113, A00A15. doi:10.1029/2008JA013224.

Jackson, B.V., Buffington, A., Hick, P.P., Wang, X., Webb, D., 2006. Preliminary three-dimensional analysis of the heliospheric response to the 28 October 2003 CME using SMEI white-light observations. J. Geophys. Res. 111, A04S91. doi:10.1029/2004JA0109.

Jackson, B.V., Hick, P.P., Buffington, A., Bisi, M.M., Kojima, M., Tokumaru, M., 2007. Comparison of the extent and mass of CME events in the interplanetary medium using IPS and SMEI Thomson scattering observations. Astron. Astrophys. Trans. 26, 477.

Kahler, S.W., 1992. Solar flares and coronal mass ejections. Ann. Rev. Astron. Astrophys. 30, 113.

Kahler, S.W., Webb, D.F., 2007. V arc interplanetary coronal mass ejections observed with the Solar Mass Ejection Imager. J. Geophys. Res. 112, A09103. doi:10.1029/2007JA012358.

Leinert, C., Link, H., Pitz, E., Salm, N., Knueppelberg, D., 1975. The Helios zodiacal light experiment E9. Raumfahrtforschung 19, 264.

Li, Y., Luhmann, J., 2006. Coronal magnetic field topology over filament channels: implication for coronal mass ejection initiations. Astrophys. J. 648, 732.

Liewer, P.C., Jong, E.M., Howard, J.R., Howard, R.A., Thompson, W.T., Culhane, J.L., Bone, L., van Driel-Gesztelyi, L., 2009. Stereoscopic analysis of the 19 May 2007 erupting filament. Solar Phys. 256, 57.

Low, B.C., 1996. Solar activity and the corona. Solar Phys. 167, 217.

Lugaz, N., Vourlidas, A., Roussev, I.I., 2009. Deriving the radial distances of wide coronal mass ejections from elongation measurements in the heliosphere—application to CME–CME interaction. Ann. Geophys. 27, 3479.

MacQueen, R.M., Csoeke-Poeckh, A., Hildner, E., House, L., Reynolds, R., Stranger, A., Tepoel, H., Wagner, W., 1980. The high altitude observatory coronagraph/polarimeter on the Solar Maximum Mission. Solar Phys. 65, 91.

Michels, D.J., Howard, R.A., Koomen, M.J., Sheeley, N.R., Jr., 1980. In: Kundu, M.R., Gergely, T.E. (Eds.), Radio Physics of the Sun, Reidel, D., Hingham, MA, p. 439.

Mierla, M., Inhester, B., Antunes, A., Boursier, Y., Byrne, J.P., Colaninno, R., Davilla, J., de Koning, C.A., Gallagher, P.T., Gissot, S., Howard, R.A., Howard, T.A., Kramar, M., Lamy, P., Liewer, P.C., Maloney, S., Marqué, C., McAteer, R.T.J., Moran, T., Rodriguez, L., Srivastava, N., St. Cyr, O.C., Stenborg, G., Temmer, M., Thernisien, A., Vourlidas, A., West, M.J., Wood, B.E., Zhukov, A.N., 2010. On the reconstruction of coronal mass ejections using coronagraph data. Ann. Geophys. 28, 203.

Mierla, M., Inhester, N., Marque, C., Rodriguez, L., Gissot, S., Zhukov, A., Berghmans, D., Davila, J., 2009. On 3D reconstruction of coronal mass ejections: I method description and application to SECCHI-COR data. Solar Phys. 259, 123.

Minnaert, M., 1930. On the continuous spectrum of the corona and its polarisation. Z. Astrophys. 1, 209.

Moran, T.G., Davila, J.M., Thompson, W.T., 2010. Three-dimensional coronal mass ejection structure and orientation from polarimetric and geometric analyses of stereoscopic observations. Astrophys. J. 712, 453.

Odstrcil, D., Riley, P., Zhao, X.P., 2003. Numerical simulation of the 12 May 1997 interplanetary CME event. J. Geophys. Res. 109, A02116. doi:10.1029/2003JA010135.

Owens, M., Cargill, P., 2004. Predictions of the arrival time of coronal mass ejections at 1 AU: an analysis of the causes of errors. Ann. Geophys. 22, 661.

Schuster, A., 1879. On the polarisation of the solar corona. Mon. Not. R. Astron. Soc. 40, 35.

Sheeley Jr., N.R., Walthers, J.H., Wang, W-M., Howard, R.A., 1999. Continuous tracking of coronal outflows: two kinds of coronal mass ejections. J. Geophys. Res. 104, 24739.

Simnett, G.M., Harrison, R.A., 1984. The relationship between coronal mass ejections and solar flares. Adv. Space Res. 4, 279.

St. Cyr, O.C., Howard, R.A., Sheeley Jr., N.R., Plunkett, S.P., Michels, D.J., Paswaters, S.E., Koomen, M.J., Simnett, G.M., Thompson, B.J., Gurman, J.B., Schwenn, R.,

Please cite this article as: Howard, T.A., Three-dimensional reconstruction of coronal mass ejections using heliospheric imager.... Journal of Atmospheric and Solar-Terrestrial Physics (2010), doi:10.1016/j.jastp.2010.08.009

Webb, X.-P., Hildner, E., Lamy, P.L., 2000. Properties of coronal mass ejections: SOHO LASCO observations from January 1996 to June 1998. J. Geophys. Res. 105, 18169.

Tappin, S.J., Buffington, A., Cooke, M.P., Eyles, C.J., Hick, P.P., Holladay, P.E., Jackson, B.V., Johnston, J.C., Kuchar, T., Mizuno, D., Mozer, J.B., Price, S., Radick, R.R., Simnett, G.M., Sinclair, D., Waltham, N.R., Webb, D.F., 2004. Tracking a major interplanetary disturbance with SMEI. Geophys. Res. Lett. 31, L02802. doi:10.1029/2003GL018766.

Tappin, S.J., Howard, T.A., 2009. Interplanetary coronal mass ejections observed in the heliosphere: 2. Model and data comparison. Space Sci. Rev. 147, 55.

Temmer, M., Preiss, S., Veronig, A., 2009. CME projection effects studied with STEREO/COR and SOHO/LASCO. Solar Phys. 256, 183.

Thernisien, A.F.R., Howard, R.A., Vourlidas, A., 2006. Modeling of flux rope coronal mass ejections. Astrophys. J. 652, 763.

Tousey, R., 1973. In: Rycroft, M.J., Runcorn, S.K. (Eds.), The Solar Corona, Space Research XIII. Akademie-Verlag, Berlin, pp. 713.

Tripathi, D., Bothmer, V., Cremades, H., 2004. The basic characteristics of EUV post-eruptive arcades and their role as tracers of coronal mass ejection source regions. Astron. Astrophys. 422, 337.

van de Hulst, H.C., 1950. The electron density of the solar corona. Bull. Astron. Inst. Neth. 11, 135.

Vourlidas, A., Howard, R.A., 2006. The proper treatment of coronal mass ejection brightness: a new methodology and implications for observations. Astrophys. J. 642, 1216.

Wang, Y., Xue, X., Shen, C., Ye, P., Wang, S., Zhang, J., 2006. Impact of major coronal mass ejections on geospace during 2005 September 7–13. Astrophys. J. 646, 625.

Wang, Y., Zhang, J., Shen, C., 2009. An analytical model probing the internal state of coronal mass ejections based on observations of their expansions and propagations. J. Geophys. Res. 114, A10104. doi:10.1029/2009JA014360.

Webb, D.F., Mizuno, D.R., Buffington, A., Cooke, M.P., Eyles, C.J., Fry, C.D., Gentile, L.C., Hick, P.P., Holladay, P.E., Howard, T.A., Hewitt, J.G., Jackson, B.V., Johnston, J.C., Kuchar, T.A., Mozer, J.B., Price, S., Radick, R.R., Simnett, G.M., Tappin, S.J., 2006. Solar mass ejection imager (SMEI) observations of coronal mass ejections (CMEs) in the heliosphere. J. Geophys. Res. 111, A12101. doi:10.1029/2006JA011655.

Webb, D.F., Howard, T.A., Fry, C.D., Kuchar, T.A., Odstrcil, D., Jackson, B.V., Bisi, M.M., Harrison, R.A., Morrill, J.S., Howard, R.A., Johnston, J.C., 2009. Study of CME propagation in the inner heliosphere: SOHO LASCO, SMEI and STEREO HI observations of the January 2007 events. Solar Phys. 256, 239.

Wood, B.E., Howard, R.A., 2009. Am empirical reconstruction of the 2008 April 26 coronal mass ejection. Astrophys. J. 702, 901.

Wood, B.E., Howard, R.A., Thernisien, A., Plunkett, S.P., Socker, D.G., 2009. Reconstructing the 3D morphology of the 2008 May 17 CME. Solar Phys. 259, 163.

Yashiro, S., Gopalswamy, N., Michalek, G., St. Cyr, O.C., Plunkett, S.P., Rich, N.B., Howard, R.A., 2004. J. Geophys. Res., A07105. doi:10.1029/2003JA010282.

Zhao, X.-P., 2008. Inversion solutions of the elliptic cone model for disk frontside full halo coronal mass ejections. J. Geophys. Res. 113, A02101. doi:10.1029/2007JA012582.

Zhao, X.-P., Plunkett, S.P., Lui, W., 2002. Determination of geometrical and kinematical properties of halo coronal mass ejections using the cone model. J. Geophys. Res. 107, 1223.

Please cite this article as: Howard, T.A., Three-dimensional reconstruction of coronal mass ejections using heliospheric imager.... Journal of Atmospheric and Solar-Terrestrial Physics (2010), doi:10.1016/j.jastp.2010.08.009